Engineering austenite/martensite mesostructured materials by controlled localised laser treatments in a Fe–Ni–C alloy

Breukelman, H. J.; Hermans, M. J.M.; Santofimia, M. J.; Hidalgo, J.

DOI
10.1016/j.matdes.2023.111772

Publication date
2023

Document Version
Final published version

Published in
Materials and Design

Materials & Design 227 (2023) 111772

Contents lists available at ScienceDirect

Materials & Design

journal homepage: www.elsevier.com/locate/matdes

Engineering austenite/martensite mesostructured materials by controlled localised laser treatments in a Fe–Ni–C alloy

H.J. Breukelman [a], M.J.M. Hermans [a], M.J. Santofimia [a], J. Hidalgo [a,b,*]

[a] Department of Materials Science and Engineering, Delft University of Technology, Mekelweg 2, 2628 CD Delft, The Netherlands
[b] Universidad de Castilla La Mancha. ETSII-INEI. DYPAM Research Group. Avda. Camilo José Cela s/n. Ciudad Real 13071, Spain

HIGHLIGHTS

- The mesostructure of α'/ γ steel was tailored by varying laser parameters.
- Gradient microstructures resulted from steep temperature and heating rate gradients.
- Formulated model predictions are in agreement with observed microstructures.
- Specimen thickness and absorptivity determine laser heat penetration.
- High heating rates produced pseudo-displacive α' → γ and recrystallization.

GRAPHICAL ABSTRACT

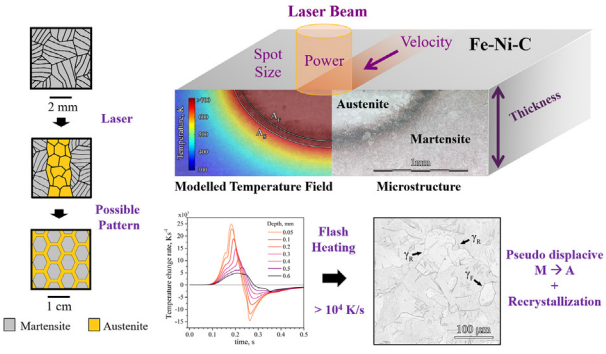

ARTICLE INFO

Article history:
Received 26 November 2022
Revised 11 February 2023
Accepted 16 February 2023
Available online 18 February 2023

Keywords:
Patterned microstructure materials
Austenite
Martensite
Local heat treatment
Flash heating

ABSTRACT

Localised laser treatments enable the creation of sophisticated austenite/martensite mesostructures in Fe–Ni–C steel with the potential of achieving enhanced mechanical performance. The control of phase topology is essential to modify the properties of these structures on demand and requires a profound understanding of the effect of the processing parameters on the development of the different phases upon the application of laser treatment. In this work, the microstructure evolution under exceptional gradients in temperature and heating rates is thoroughly investigated. The extent of the laser-affected zone and the heat input were tailored by varying laser parameters and specimen thickness, based on a model that considers transient material properties and the coupling between temperature and microstructure. The predicted temperature fields resulted in a complex interplay between martensite to austenite phase transformation and martensite tempering. Considering the high heating rates of up to 25000 K/s and the observed microstructures, it is suggested that austenite was formed by a pseudo-displacive mechanism and subsequently fully recrystallised in the zones most directly affected by the laser heat source. A smooth strength transition from austenite to martensite, affected by the laser parameters, could be exploited for more effective deformation mechanisms and improved material mechanical properties.

1. Introduction

Laser treatment is a widely used and well-established technology in surface engineering because of its benefits over traditional surface treatment methods [1,2]. Laser treatments permit fast processing with high accuracy and localization of microstructure mod-

* Corresponding author.
E-mail address: J.HidalgoGarcia@tudelft.nl (J. Hidalgo).

https://doi.org/10.1016/j.matdes.2023.111772
0264-1275/

ification by solid-state phase transformations of the near-surface regions of materials. Making use of the fast heat release and heat redistribution in metals, self-quenching conditions can be reached to form martensite after applying a laser treatment over a ferritic steel base material pursuing a surface hardening [3,4]. Lasers can be also used for tempering, which can be exploited in tool steel to produce a secondary hardening [5]. On the contrary, laser treatment can result in a softening, e.g, in titanium alloy microstructures to improve their machinability [6].

In all these applications, a homogenous microstructure along the material surface is sought and the microstructure only varies in the direction of the material bulk. However, laser treatment has been explored to create more sophisticated microstructures in steel. Using shadow masks of different geometries, Andreev et al. [7] and Pimenov et al. [8] produced gradient microstructures in a Fe-Cr-Ni metastable austenitic steel by restoring a base cold-rolled martensitic microstructure by laser treatment. Breukelman et al. [9] also explored this concept to create patterned austenite/-martensite mesostructures in Fe–Ni–C metastable austenitic steel. Base martensitic microstructures were developed by a cryogenic treatment, in which the strength of martensite was adjusted by tempering. The authors demonstrated that by playing with the austenite/martensite topology and the properties of the constitutive phases in the mesostructure created by the laser, the macroscopic properties of these steels can be modified on demand. These studies open new possibilities for using laser treatments for dictating the microstructure of metal alloys in distinctive mesostructure topologies with the capacity to reach exceptional properties.

Fe–Ni–C steels have been extensively studied for the understanding of steel transformation mechanisms and kinetics depending on temperature variation rates and the application of strain [10–12]. Mechanical induced austenite to martensite transformation provides Fe–Ni–C metastable austenitic compositions of high work hardening and meritorious strength and uniform elongation [9,12,13]. Good mechanical properties are maintained for the duplex austenitic/martensitic microstructures formed upon cooling to temperatures below room temperature or ausforming [9,14]. Upon rapid heating, martensite to austenite reversion in these steels is reported to result in austenitic microstructures with high thermal and mechanical stability and enhanced mechanical properties [10,15,16]. This calls for exploring new processing routes of Fe–Ni–C austenitic steels involving rapid heating from martensitic microstructures. High heating rates are typically achieved by induction heating. The application of laser treatments, producing highly local and surface-only extreme temperature variations in a short time, has been seldom studied in Fe–Ni–C steels.

Transient temperature fields with pronounced temperature gradients will produce gradient microstructures in the laser-affected zone (LAZ) of base martensite microstructures in Fe–C–Ni steels. The microstructure will transit from: 1) reverted austenite at regions affected by the laser heat to the extent of raising local temperature to above the austinitisation point, 2) prassing through regions consisting of duplex microstructures or tempered martensite as the peak temperature decreases from the laser spot, 3) to the base martensitic microstructure unaffected by the laser heat source. The width and depth of the regions affected by the laser are mainly determined by the energy density supplied by the laser, tailored by varying process parameters, and heat release or redistribution mechanisms (e.g. self-quenching) are determined by the specimen geometry. Controlling the temperature field and understanding the effect of laser treatments on the material structure at different scales will enable the full benefit of the creation of patterned mesostructured austenite/martensite Fe–Ni–C steels for improved mechanical properties.

Obtaining accurate information on temperature and heating rates as a function of location in the workpiece (x,y,z) and time (t) is a challenging issue concerning measurements, especially in the workpiece interior. The increase in computational power in the last decades is making the use of models a powerful tool in this respect. For a complete macro- or mesoscale model of heat treatments in steel, i.e. a model that addresses the heat treatment in terms of phase domains rather than on microscale features, a system including the coupling between the thermal, microstructural and mechanical state of steel needs to be considered. Bailey et al. [17], collectively referred to this system as the Metallo-Thermo-Mechanical (MTM) coupling system which is represented in Fig. 1a. These couplings demonstrate, e.g, that a given stress state, can induce a phase transformation (coupling number 5), which in turn influences the temperature field through a change in thermal properties (coupling number 4). The central role of carbon in Fig. 1a emphasises its effect on transformation kinetics (microstructure change) and dislocation movement (strain/stress) and indirectly on temperature by the different coupling effects.

The literature contains some interesting attempts to model the MTM coupling system. Bailey et al. [17], proposed a model for residual stress in AISI 4140 steel after laser hardening, which solves the thermal field using an implicit finite volume method, while simultaneously calculating phase transformation kinetics and carbon diffusion. However, the effect of the microstructural change on the thermal field, through e.g. latent heat, is neglected. Patwa and Shin [18], posit a finite volume thermal-kinetic model for AISI5150H, with constant density, and temperature-dependent heat capacity and conductivity in the interval between 300 K and 1100 K, and a similar pearlite dissolution kinetics approach as [4]. The thermal model does not consider other parameters relevant to microstructural changes, such as heating rate. Mioković *et al.*, [19] developed a finite element model in which microstructural changes were implemented based on TTT diagrams for AISI 4140. Heat capacity and latent heat, conductivity, and density are included in the model as phase-dependent parameters. Although interesting, the simplifications regarding the model geometry and heat source limit the practical applications of this model for laser-architectured microstructures. Telrandhe *et al.* [6], showed the effect of heat build-up in the workpiece on penetration depth during laser heat treatment of Ti6Al4V. They formulated the heat equation with heat capacity and conductivity as temperature-dependent parameters, alongside explicit modelling of the laser heat source as a volume flux, as developed by Goldak *et al.* [20]. Furthermore, an attempt is made to establish the effect of laser process parameters, specifically scanning speed, on absorptivity. While the absorptivity could be considered strictly as a (temperature-dependent) parameter of the material surface, this coupling between the process and the material offers an interesting alternative approach.

The present work analyses the effect of laser parameters and workpiece thickness on the microstructures and extent of the LAZ of a Fe–Ni–C alloy with a martensitic base microstructure. A detailed characterisation of the microstructure evolution under the exceptional gradients in temperature and heating rate inherent to laser processing is performed. To assist the interpretation of the resulting microstructures, the laser process is modelled following an MTM coupling system such as the one indicated in Fig. 1b, which in conjunction with the phase change hysteresis for thermal parameters, constitutes a novel approach to modelling laser treatments in materials exhibiting solid-state transformations. The model is validated by comparing its output with the microstructure along the laser-affected zone and the microstructures resulting from dilatometry experiments. Based on the results, the challenges associated with the implementation of laser treatments

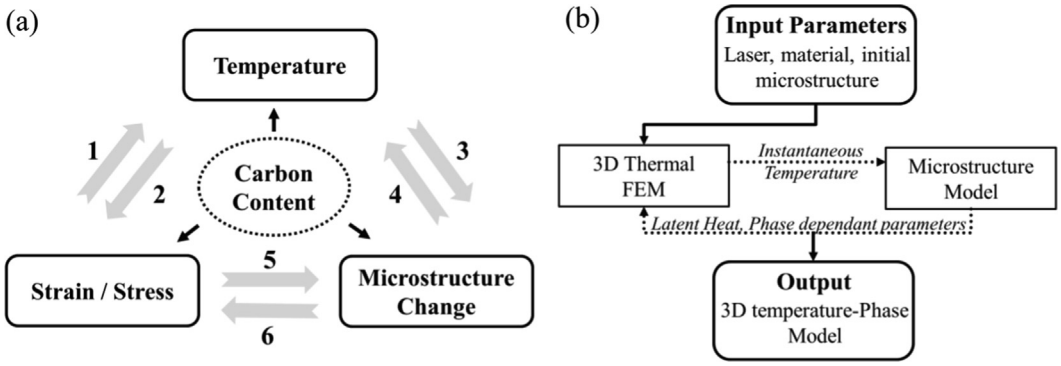

Fig. 1. (a) Metallo-Thermo-Mechanical coupling diagram drawn after (Bailey et al., 2009). 1: Mechanical heat, 2: Thermal strain, 3: Phase transformation, 4: Latent heat, 5: Stress-induced phase transformation, 6: Dilatation strain. (b) Scheme of the current model.

for the creation of controlled mesostructures in metal alloys are discussed.

2. Modelling laser treatments

A Finite Element Model (FEM) was defined in COMSOL Multiphysics® 5.3a to resolve the transient temperature development in a 3D geometry. The temperature field was modelled using the time-dependent heat equation, considering a laser heat flux based on the control parameters of the laser equipment: Power (P), the focal-spot diameter (d_s) and velocity of the laser relative to the workpiece (v). A full description of the parameters used, as well as equipment and environmental constants assumed and defined, can be found in a Data in Brief attached to this paper [21].

The temperature (T) variation over time (t) in the volume domain is formulated as:

$$\frac{\partial T}{\partial t} = \frac{k}{\rho C_p}\left(\frac{\partial^2 T}{\partial y^2} + \frac{\partial^2 T}{\partial y^2} + \frac{\partial^2 T}{\partial z^2}\right) + \frac{q}{\rho C_p} \quad (1)$$

where the parameter q is the heat flux in the domain under consideration. Eq.(1) contains three material parameters, heat conductivity (κ), specific heat capacity at constant pressure (C_P) and density (ρ). These parameters are dependent on the temperature and microstructural phase, and therefore have to be considered in light of a phase change model for the case of the laser heat treatment proposed in this work. This phase change, implemented using COMSOL's Domain Ordinary Differential Equation functionality, compels the use of a specific set of parameters based on the thermal history of the model element.

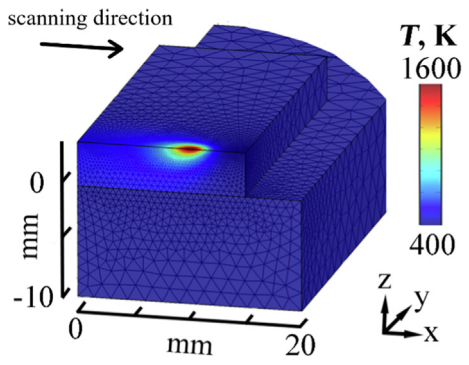

Fig. 2. Three-dimensional representation of the modelled laser set-up and temperature fields for a 4 mm thick workpiece resting on a cooper contact block at a time frame when the laser is crossing its width (y-axis).

Fig. 2 shows an example of the model outcome. The figure shows a three-dimensional representation of the workpiece at a time frame when the laser is crossing its width. The specimen is resting on a copper contact block that dissipates heat by conduction. Radiation and convective boundary conditions are also implemented to model the heat transfer from the sample to the environment. A detailed description of the boundary condition can be found elsewhere in Data in Brief accompanying this paper [21].

The fine mesh size along the laser spot's trajectory was defined to gain accuracy in the temperature prediction and to adequately resolve the highly localised laser heat flux. The mesh size becomes rougher in regions far from the laser influence to gain computation efficiency. The colour scale is coded by different temperatures reached along its geometry. Only half of the workpiece is shown due to symmetry along the x-z plane.

Thermal measurements and sensitivity analysis of the absorptivity of the workpiece were carried out and the validity of the model is discussed in subsequent sections.

3. Materials and methods

3.1. Material and specimen preparation

A metastable austenitic steel with a composition of 0.2C-25Ni-0.02Mn wt.% is selected for the study. The alloy exhibits a fully austenitic microstructure at room temperature, which can be turned into a martensitic microstructure by a quenching treatment in liquid nitrogen (77 K).

The alloy was vacuum cast in an 80 mm × 80 mm × 400 mm billet that was subsequently forged to a 50 mm × 50 mm × 1000 mm billet and homogenised at 1273 K for 12 h. Dilatometry cylindrical specimens (Fig. 3a) and flat coupons (Fig. 3b) of 1 mm and 4 mm thickness were machined from the billet. All machined specimens were subjected to an alkali chloride salt bath treatment at 1200 K for 600 s to develop an austenitic microstructure. Thereafter, specimens were immersed in liquid nitrogen for 300 s to obtain a fully martensitic base microstructure.

3.2. Application of heat treatments by laser and dilatometry.

A Trumpf HL3006D Nd:YAG laser with a continuous wave pulse at a wavelength of 1064 nm and a focal length of 170 mm was used for the localised laser treatments. Specimens surfaces were ground up to a P80 sandpaper grit finish to mitigate the risk of specular reflection of laser radiation. The schematic of the experimental setting is shown in Fig. 3c. The laser parameters P, v and d_s were varied to assess their effect on the microstructure and extension of the

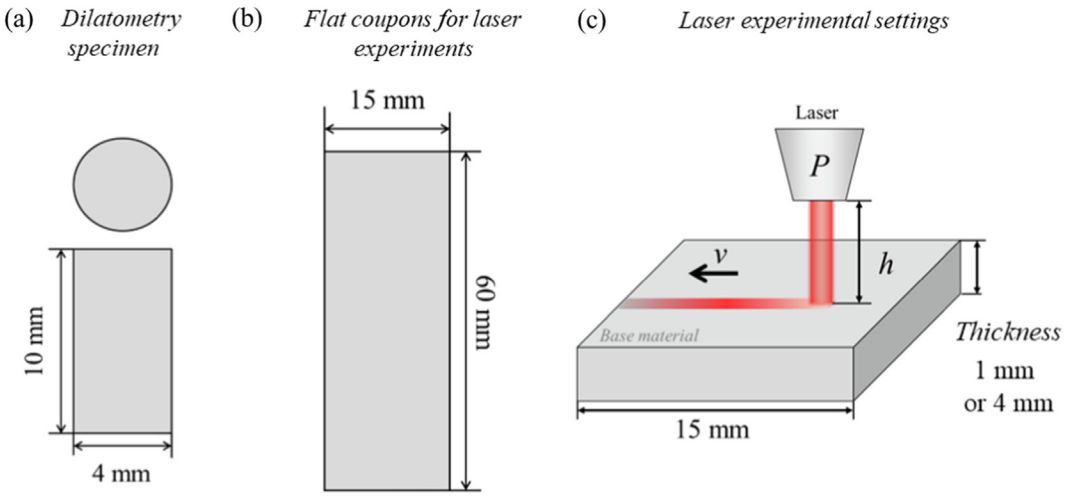

Fig. 3. Scheme of different machined specimens: (a) dilatometry specimens, (b) flat coupons for laser experiments, together with (c) laser experimental settings.

laser-affected zone (LAZ). The area projected by the laser beam on the specimen surface is regulated by the change in the height of the laser source concerning the flat workpiece, h, considering that d_s was at its minimum of approximately 0.45 mm for a height of 170 mm, 0.78 mm for a height 180 mm and 1.02 mm for a height of 190 mm. During laser treatments, temperature measurements were conducted using K-type thermocouples positioned at different distances from the heat-treated areas.

To have a better understanding of the microstructures developed during laser treatments, additional heat treatments mimicking localised heat treatments in specific parts of the specimen were carried out in a Bähr DIL 805 A/D/T dilatometer. A vacuum atmosphere ($2{\cdot}10^{-5}$ bar) was maintained during heating. A K-type thermocouple was spot welded to the middle of the dilatometer specimen surface for temperature control. Heat treatments consisted of heating solid dilatometry specimens at 100 K/s to temperatures varying from 473 K to 1373 K in 100 K steps followed by an isothermal time of 2 s before they were cooled down by helium gas at a rate of 100 K/s.

3.3. Microstructure characterisation

Specimens, both laser treatments and dilatometry, were metallographically prepared by grinding and polishing to 1 μm diamond paste for microstructure characterisation. To reveal the austenitic microstructure, specimens were etched with waterless Kalling's #2 reagent (5 gr $CuCl_2$ + 100 ml of HCl at 33% + 100 ml Ethyl alcohol). Nital 2% etching was used to reveal the martensitic microstructure. Light optical microscopy (LOM) was performed using a Leica DMLM and a Keyence VHX-100 digital microscope. A JEOL JSM-6500F scanning electron microscope (SEM) in secondary imagining detection mode was used for a detailed characterisation of the microstructures. Hardness Vickers HV0.2 was measured in an EMCO G5 DuraScan.

To determine the retained austenite fraction after cryogenic treatment, X-ray diffraction measurements were carried out in a Bruker D8 Advance diffractometer in Bragg-Brentano geometry with a graphite monochromator and Vantec position-sensitive detector. Cobalt radiation was used to obtain a diffractogram covering 20°−135° with a step size of 0.021° 2θ and counting time per step 2 s. Rietveld refinement was used in the peak identification and quantification of phase fractions. The peaks {111}, {200}, {220}, {311} and {222} for austenite and {110}, {200}, {211} and {220} for martensite were analysed.

4. Results

4.1. Base materials characterisation

Fig. 4a shows a micrograph of the base austenitic microstructure. An average austenite grain size of 72 ± 4 μm was obtained after the analysis of more than 100 grains by ImageJ software based on a methodology described in [22]. A large population of twins is observed in the microstructure. Some martensite formation is noticed close to the specimen surface.

After quenching in liquid nitrogen, butterfly-type martensite is formed (Fig. 4b). XRD analysis revealed a 0.08 ± 0.01 fraction of austenite in this microstructure. Umemoto and Tamura [23], reported that this type of martensite can form in various ferrous alloys and typically consists of two butterfly wings, each one constituting a single twin pair of martensite with a relative misorientation angle of 16°. Sato and Zaefferer [24] and Apple and Krauss [25] made a similar description of butterfly martensite formed below room temperature in a Fe–30Ni wt.% alloy and a Fe–25Ni–0.3C wt.% alloy, respectively.

A specimen with the described martensitic microstructure was tempered by heating it to 523 K during 1800 s in a sodium nitrite salt bath to characterise the microstructure changes occurring in martensite upon moderate heating. As shown in Fig. 4c, white-etched butterfly wings are not clearly distinguishable any longer, and the microstructure turned brownish likely due to the formation of carbides. The hardness $HV_{0.2}$ of the initial austenitic, martensitic and tempered martensitic microstructures are 212 ± 15, 387 ± 10 and 353 ± 12, respectively.

4.2. Dilatometry experiments.

It is important to understand the characteristics of martensitic and austenitic microstructures that can be developed at different temperatures in the present material, to facilitate the identification of microstructures and properties of the laser-treated zones. With that aim, dilatometry experiments reaching different target top temperatures were carried out, followed by cooling at 100 K/s. The resulting specimens' microstructure and hardness were determined so they can be compared to those developed at different points of the laser-treated material.

Fig. 5 shows the experimentally measured hardness of these dilatometry specimens as a function of the top temperatures, in which the martensite to austenite start, A_s, and finish, A_f, tempera-

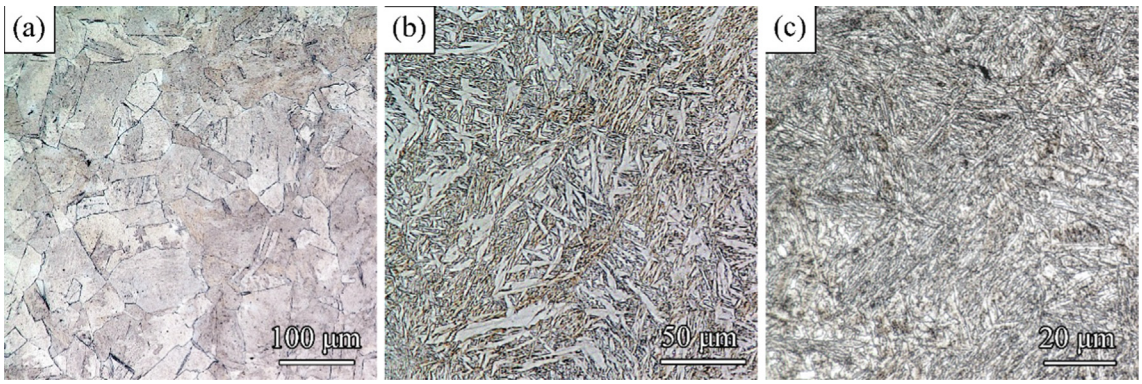

Fig. 4. (a) Initial austenitic microstructure. (b) Martensitic microstructure after cryogenic treatment in liquid nitrogen. (c) Tempered martensite microstructure.

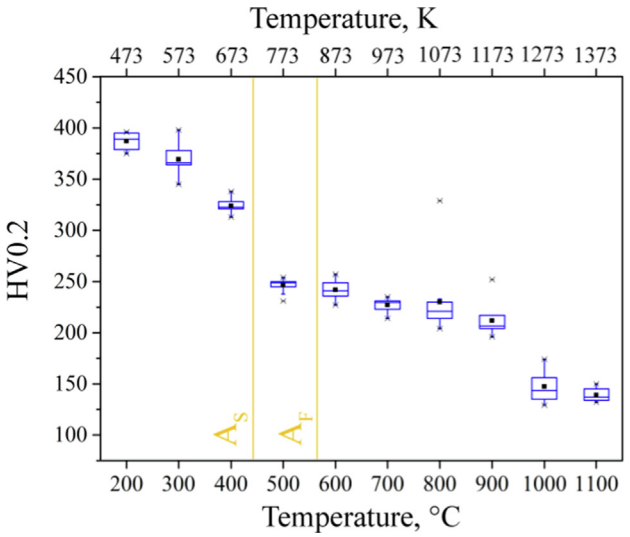

Fig. 5. Hardness at different temperature steps of dilatometry specimens. The boxes are delimited by the lower and upper quartiles, Q1 and Q3, respectively, and the line crossing through them is the data median, Q2. The end of the whisker marks off the lowest datum within 1.5 times IQR (IQR = Q3- Q1) below Q1 and the highest datum within 1.5 times IQR above Q3. The symbol "*" represents the maximum and minimum values.

tures obtained from the dilatometer at 100 K/s heating rate are specified. In the temperature interval from room temperature to A_s, the hardness monotonically decreases with increasing temperature. Since the peak temperature for these three experiments is below A_s, there is no formation of austenite, and the reduction of hardness is attributed to martensite tempering. Bhadeshia and Honeycombe [26] describe steel tempering as involving the segregation of interstitial carbon, carbide formation and possibly a decrease of dislocation density, all resulting in a reduction of hardness. When the top temperature reaches A_s, there is a significant drop in hardness due to austenite formation, which remains the stable phase at room temperature. The hardness decrease with increasing temperature for the temperature range above A_f can be attributed to the recovery and recrystallization of austenite.

The microstructure obtained after cooling from a peak temperature of 1073 K is shown in Fig. 6a. This microstructure adequately represents the characteristic microstructural features observed after cooling for heat treatments with peak temperature in the 873 K to 1173 K temperature interval. A light grey-etched austenitic microstructure is developed with the sporadic observation of brownish butterfly martensite wings. A hierarchical microstructure is observed in which big austenite grains of more than 100 µm size seem to be fragmented into smaller grains resembling packets. A big population of twin-like features are also visible, but the continuity of parallel facets seems at times interrupted. Krauss [11], referred to these features as reversal twins and proposed that they are derived from martensitic plates arranged in more or less parallel groups. Wavy austenite grain boundaries (wb) are commonly observed as if they were outlined by a combination of prior butterfly martensite wings. A prior butterfly martensite (γ_{BM}) shape is maintained by some austenite grains, as indicated in Fig. 6a.

Fig. 6b shows the austenitic microstructure obtained at 1273 K. Wavy austenite grain boundaries appear to be blunted into a more curved shape. Some austenite grains appeared to be fragmented into smaller subgrains that are lightly etched (γ_F). Austenite grains of less than 10 µm were also sporadically observed next to coarser austenite grains as indicated by arrows (γ_R). These small grains are likely recrystallized austenite grains.

4.3. Microstructure at the LAZ

In this section, the microstructures developed along the LAZ of the 4 mm-thickness specimens are analysed for a selected combination of laser parameters shown in Table 1. The laser spot diameter is 0.78 mm in all conditions. All these conditions are extracted from a preliminary study in which 20 laser set-up parameters were experimentally investigated following a factorial design of experiments. This study can be consulted in the Data in Brief, accompanying this paper [21]. The selected conditions do not exhibit melting and result in homogeneous and visible development of an austenite region at the LAZ both at the surface and penetrating the specimens. In Table 1, the linear energy, a common metric [27,28] to describe energy input in laser welding is included, defined as:

$$E_L = \frac{\eta P}{v} \tag{2}$$

where η denotes the process efficiency, which is assumed to be constant (η = 1) for all conditions. The linear energy facilitates a comparison between the four laser lines, demonstrating that although laser power was significantly higher in Line 1 and Line 2, the slower workpiece velocity should result in more energy deposition in the case of Line 3 and Line 4.

Fig. 7a shows the microstructure at the surface of the laser Line 1. The straight path of the laser-affected zone can be distinguished. Adjacent to this zone, several well-differentiated regions with characteristic microstructural features were observed in the magnified micrograph of Fig. 7b. The region most directly affected by the laser beam, Z1 in Fig. 7c, exhibits an austenitic microstructure with a small grain size (24 ± 1 µm) which develops along 1.3 mm.

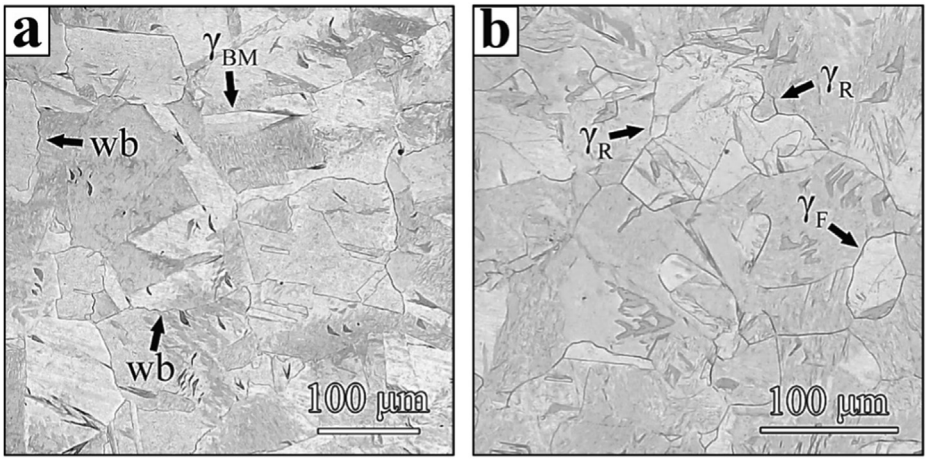

Fig. 6. Light optical microscopy images of microstructures obtained by dilatometry after heating at 100 K/s to (a) 1073 K and (b) 1273 K, followed by cooling to room temperature. wb = wavy boundaries, γ_{BM} = austenite grain retaining the shape of prior butterfly martensite, γ_R = recrystallized austenite grain, γ_F = fragmented austenite grain.

Table 1
Laser experiment parameters power (P), working piece speed (v), and linear energy (E_L) of four selected laser lines for a constant laser diameter d_s = 0.78 mm.

	P (W)	v (mm/s)	E_L (J/mm)
Line 1	400	25	16
Line 2	400	20	20
Line 3	200	5	40
Line 4	200	2.5	80

The adjacent region, Z2 in Fig. 7c, consists of large austenite grains with 172 ± 7 μm average size and extends 0.35 mm from the limits of Z1. A dark etched region of 0.2 mm, Z3 in Fig. 3c, delimits the frontier between the central austenitic region and the bulk martensitic microstructure. The frontier between Z2 and Z3 regions defines the A_f isotherm line in experimental observations.

The hardness HV0.2 profile, shown in Fig. 7c, is explained by the regions delimited in the microstructure analysis. Forouzan et al. [29] studied the hardness dependence of submicron-grained austenitic steel and concluded that the Hall-Petch relation holds down to at least 300 nm of grain size. Remarkably, the HV0.2 of small austenite grains in the present study is less than that of large austenite grains, which contradicts the Hall-Petch relation prevalent in austenitic steels for such a grain size interval. However, the hardness matched well with that measured in the dilatometer specimens for temperatures higher than 1173 K. A plausible explanation for the low hardness in Z1 is a decrease in dislocation density by recovery and recrystallization, which is in line with the observation of small austenite grain sizes. Hardness progressively increases from the dark etched region (Z3) to the base as-quenched martensitic microstructure.

The microstructure at the surface of Line 2, Line 3 and Line 4 exhibit the same zonation described for Line 1, as shown in LOM micrographs coupled with hardness profiles of Fig. 8 a to c. The extent of these regions varies depending on the laser parameters and is gathered in Table 2. The ratio of different zones' widths, Z1/(Z1 + Z2), is 0.65, 0.77, 0.64, and 0.64 for Lines 1, 2, 3 and 4, respectively. Apart from Line 2 and considering experimental inaccuracies, this ratio does not significantly vary for different lines, which for the selected laser conditions suggests that the ratio is independent of the combination of parameters.

Fig. 9a (right-side) shows the specimen cross-section normal to the laser line of Line 1. The left side of this figure shows model results that will be explained in the next section. The microstructure at the laser-affected zone exhibits similarities with the specimen surface, but different zones develop radially. Below the surface, the region with small austenite grain sizes penetrates 150 μm through the specimen bulk and large austenite grains dominate in the austenitic region of the LAZ. Butterfly martensite

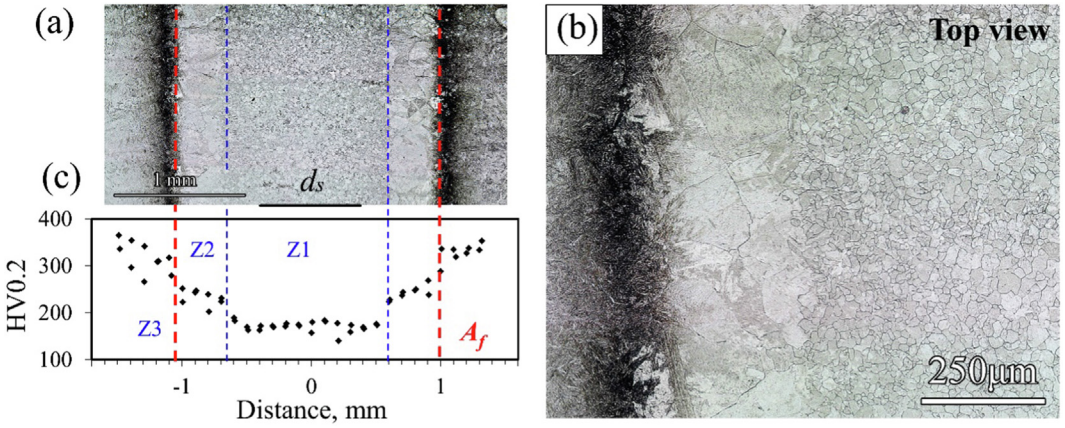

Fig. 7. (a) Light optical micrograph showing an overview of the Line 1 LAZ microstructure at the surface of the 4 mm specimen. (b) Magnified image. (c) Hardness (HV0.2) profile along the direction perpendicular to the laser travel direction.

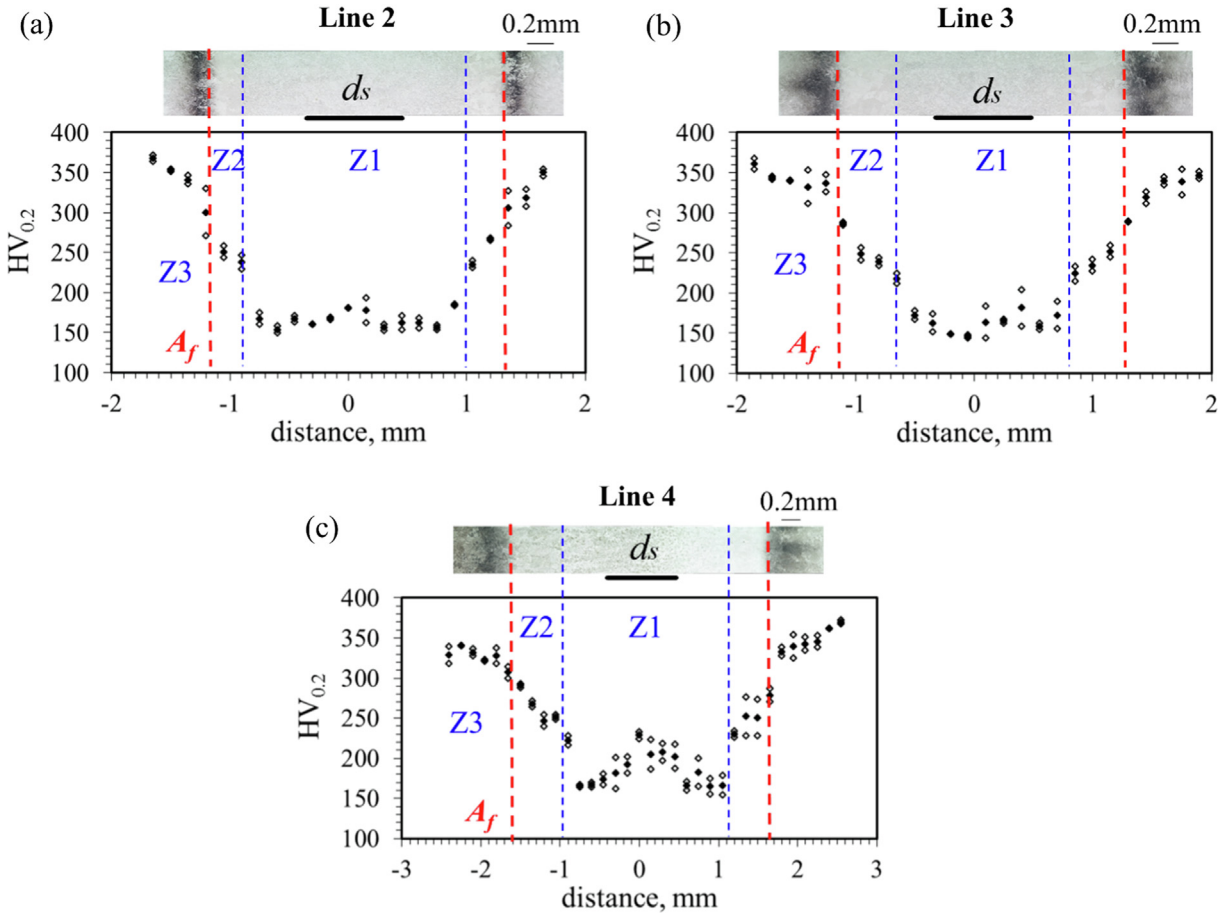

Fig. 8. Hardness (HV0.2) profile along the perpendicular direction to the laser line coupled with light optical micrographs of LAZ at specimen surface for (a) Line 2, (b) Line 3 and (c) Line 4.

Table 2
Modelled and experimental extension of the different zones in the austenitic region at LAZ (Region B in Table 1). The divergence between modelled and experimental values in percentage is shown in (±). The error of experimental determination of different regions is estimated to be ±0.1 mm. In the simulated results, A_f is considered 800 K.

		$T > A_f$ (simulated)			$T > A_f$ (experimental)		
		Width (mm)	**Depth (mm)**	$T_{at\ Z1}$ **(K)**	**Width (Z1 + Z2) (mm)**	**Width (Z1) (mm)**	**Depth (Z1 + Z2) (mm)**
$T > A_f$ Z1+Z2 Z1 Surface	**Line 1**	2.28 (+13%)	0.52 (+8%)	1412	2.01	1.3	0.48
$T > A_f$ Z1+Z2 Cross	**Line 2**	2.33 (+5%)	0.63 (+3%)	1316	2.22	1.8	0.61
	Line 3	2.28 (+4%)	0.62 (+5%)	1430	2.19	1.4	0.59
	Line 4	2.93 (-7%)	0.96 (-10%)	1328	3.15	2.0	1.07

wings are sporadically observed within austenite grains near the surface. A magnified micrograph of Fig. 9b reveals that the dark etched region consists of butterfly martensite with a blueish tone, probably as a result of carbide precipitation, and a white etched feature, likely austenite.

Fig. 10 shows a magnified SEM micrograph of the microstructure of the interface region, in which needle-like carbides are present along the transformation twins in butterfly wings and lenticular martensite. Blocks and films of retained austenite are also observed. As the base as-quenched martensite region is approached, the butterfly martensite wings turn brownish in Fig. 9b, similar to the observation in the tempered martensitic microstructure of Fig. 4c, and the population of white etched islands decreases. Far from the LAZ, the martensitic microstructure

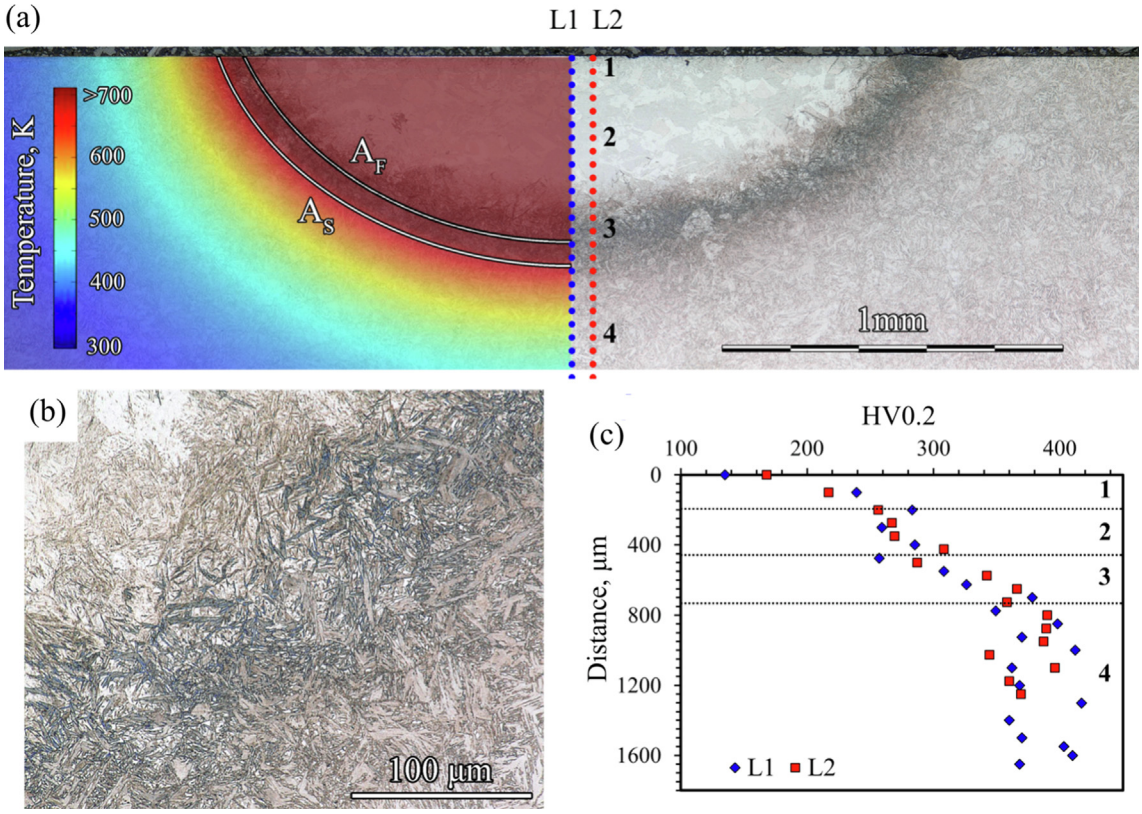

Fig. 9. (a) Light optical microscope image of the cross-section of the LAZ together with the temperature field predicted by the thermal model. (b) Magnified image showing the transition between fully austenitic and fully martensitic regions. (c) Hardness profile along the blue and red dotted lines for Line 1, and Line 2, in (a). The different regions are referred to as 1 to 4 and correspond to Z1, Z2, Z3 and base material respectively. (For interpretation of the references to colour in this figure legend, the reader is referred to the web version of this article.)

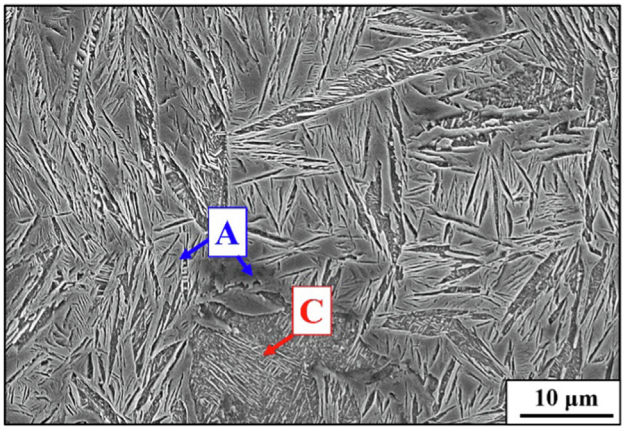

Fig. 10. SEM micrograph of the interface region between austenitic and base martensitic microstructure. Carbides are pointed by C and austenite by A.

exhibits a lighter colour comparable to the as-quenched microstructure in Fig. 9b.

Hardness monotonically increases along with the specimen depth, as can be seen in Fig. 9c, until reaching the maximum hardness in the as-quenched martensite. Along the first 200 µm from the surface, the hardness increases abruptly. This region coincides with the observation of small austenite grains. The hardness profile near the surface is likely explained by decarburization as the austenite grain size does not extensively vary in this region. Hardness remains relatively constant between 200 µm to 450 µm coinciding with the large austenite grains region. A similar description can be made for the rest of the laser lines. The measured maximum penetration depth of the austenite region of the four different studied lines can be consulted in Table 2.

4.4. Modelled temperature fields

In this section, the modelled temperature fields and heating rates of the four selected laser conditions (Table 1) are presented and the accuracy of the model is assessed. Line 1 is simulated over two different thicknesses, 1 mm and 4 mm, to analyse the effect of thickness on the resulting temperature fields.

Fig. 11a shows the simulated temperature fields over the surface of a 4 mm thickness specimen subjected to the selected combinations of laser parameters. The maximum of the colour scale indicates temperatures higher than 800 K, which corresponds to the A_f measured using a dilatometry specimen heated at 100 K/s. The predicted widths of the austenitic region are shown in Table 2. The shape of the temperature field at a specific time varies with laser conditions, with an oval contour for high workpiece velocities and a more circular one for low velocities. Temperature gradients will result in microstructure gradients in the laser-affected zone.

It is difficult to experimentally measure peak temperatures directly at the laser focus. Modelled peak temperatures resulted to be as high as 2000 K in the case of Line 2, and in general similar to or higher than 1733 K, which is the melting temperature predicted by ThermoCalc®. The absence of melting traces at the different specimen surfaces is not sufficient to discard that model-predicted peak temperature were not achieved. Peak temperatures only last a few centiseconds and melting kinetics may lag behind laser rapid temperature changes.

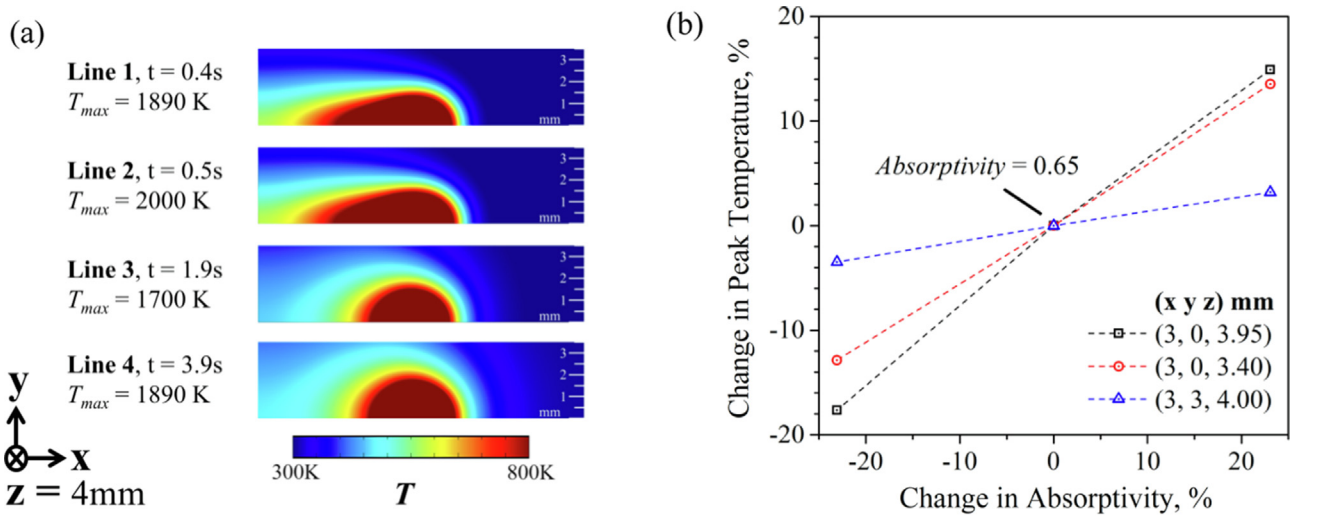

Fig. 11. (a) Top-view (specimen surface) of the modelled temperature fields for the four different laser lines. (b) Sensitivity analysis of the effect of change in absorptivity in the change of peak temperature at different locations.

Model accuracy relies on the selection of absorptivity and latent heat of the martensite to austenite phase transformation, for which an estimation had to be made due to limited available data. To investigate the effect of these estimates, a sensitivity analysis was carried out. In Fig. 11b, the model sensitivity to absorptivity is shown. Bergström [30], reported an absorptivity range of 0.5–0.8 for a variety of steels and surface conditions. Based on this study, the absorptivity was varied within this range in the present analysis. The middle of this range, with an absorptivity of 0.65, was taken as the reference point. As can be seen, the peak temperatures at different locations of the LAZ are strongly influenced by variations in absorptivity. A miscalculation of ±10 % of absorptivity shows an increase of ±6–8 % of peak temperature at points close to the laser focus, i.e. 120–160 K. Nevertheless, the peak temperature is less sensitive to variation of absorptivity as the distance to the focal point increases. The effect of latent heat on the model outputs was shown to be very limited, with changes in peak temperatures at regions close to the laser focus of less than 5 % for a variation of 60% in the reference latent heat of 19.7 kJ/kg.

Current progress in material development and structural design has enabled a reduction of component thickness. The achievement of an austenitic region that spreads out all over the specimen thickness will be critical for the development of patterned microstructures in engineering applications such as body-in-white steel components used in the automotive industry. In Fig. 12a, the effect of thickness, on the modelled thermal field is demonstrated by comparing the different penetration depths of Line 1 conditions for thicknesses of 1 and 4 mm. Along the cross-section, the temperature field is radial, though it is more flattened in the 4 mm than in the 1 mm specimen. Full-depth austenitisation is predicted to be achieved in the 1 mm thick specimen, in contrast to the 0.47 mm depth in the 4 mm specimen. This full-thickness penetration was experimentally validated in Ref [9]. The predicted maximum penetration depth of the austenitic region for the rest of the laser lines applied in the 4 mm thickness specimens is shown in Table 2.

A validation measurement of temperature variation over time was carried out on a 1 mm sample subjected to the Line 1 condition. Two thermocouples were placed on a specimen: 3 mm from the laser spot centre (Thermocouple 1), and directly below the laser spot centre (Thermocouple 2), as shown in Fig. 12b. The peak temperature of Thermocouple 1 reached 500 K and Thermocouple 2, 820 K. These temperatures are in line with the temperatures predicted by the model in Fig. 12a, which validates the model predictions and demonstrates that full penetration of austenitic regions can be achieved in sheets with a thickness of up to several millimetres. A peak temperature variation of ±2 % is predicted at Thermocouple 1 position when absorptivity is varied by 10 % (see Fig. 12b), which is a reasonable error considering the uncertainty in the value of absorptivity.

It is well known that the martensite-to-austenite transformation mechanism differs depending on the heating rate [10], which will strongly influence the final microstructure and mechanical properties of the austenite. Heating rates at different locations can be assessed through the thermal model. Fig. 13 shows the experimental and simulated temperature change rates over time at the position of the two thermocouples in the 1 mm thickness specimen. Similar trends are followed by both curves. However, predicted maximum heating rates are lower than that experimentally recorded, while temperature decreases faster in simulated specimens. It should be noted that the experimental record of Thermocouple 1 shows a limited quenching rate of 25 K/s, whereas Thermocouple 2 registered a maximum of 475 K/s. Despite some obvious differences in the experimental and simulated results, it can be concluded that simulations can give a good estimation of the order of magnitude of the heating rate at specific points of the laser-treated specimen, which would be very challenging to obtain directly by experimental methods at the laser focal point.

5. Discussion

5.1. Assessment of temperature fields at LAZ

The thermal FEM results, presented in sections 4.3 and 4.4, should suffice for an order-of-magnitude estimate of the heating rates and peak temperatures that occur in the laser heat treatment.

Absolute peak temperature in the laser-affected zone, as shown in Fig. 11a, shows a consistent overestimation of temperature at the laser focal point by the model. No melting was observed in optical micrographs of either top view or cross-section samples, despite modelled peak temperatures above the melting temperature of the alloy. This might be due to prohibitively short residence times at these temperatures, resulting in kinetic limitations on melt formation, or due to insufficient mesh refinement in the laser spot area of the FEM model. However, the comparison of width and depth of the Z1 + Z2 zone as measured by optical microscopy, compared to model prediction using a static Af of 800 K, shows agree-

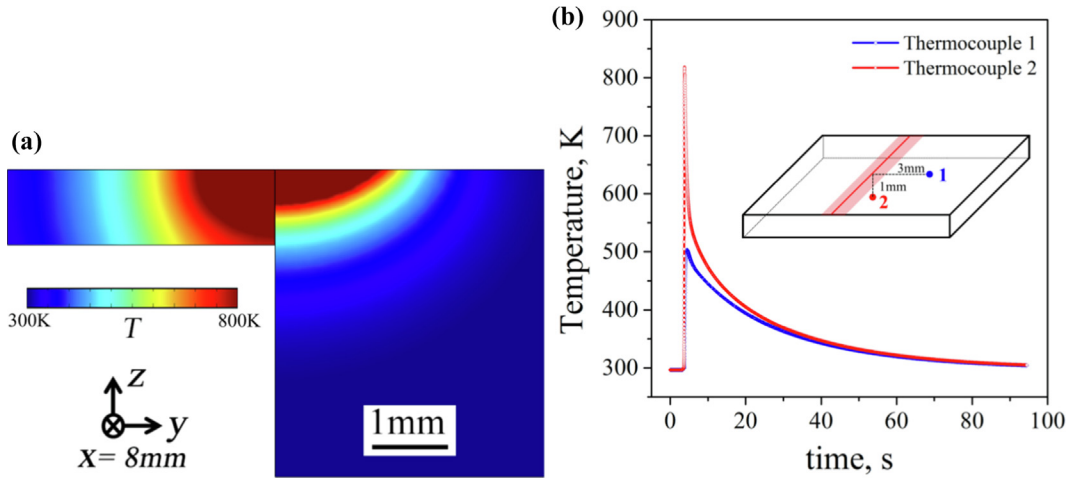

Fig. 12. (a) Modelled temperature fields at the cross-section of 1 mm and 4 mm specimens. (b) Temperature versus time was measured by two different thermocouples placed at different positions of the 1 mm specimen during the application of Line 1 laser conditions.

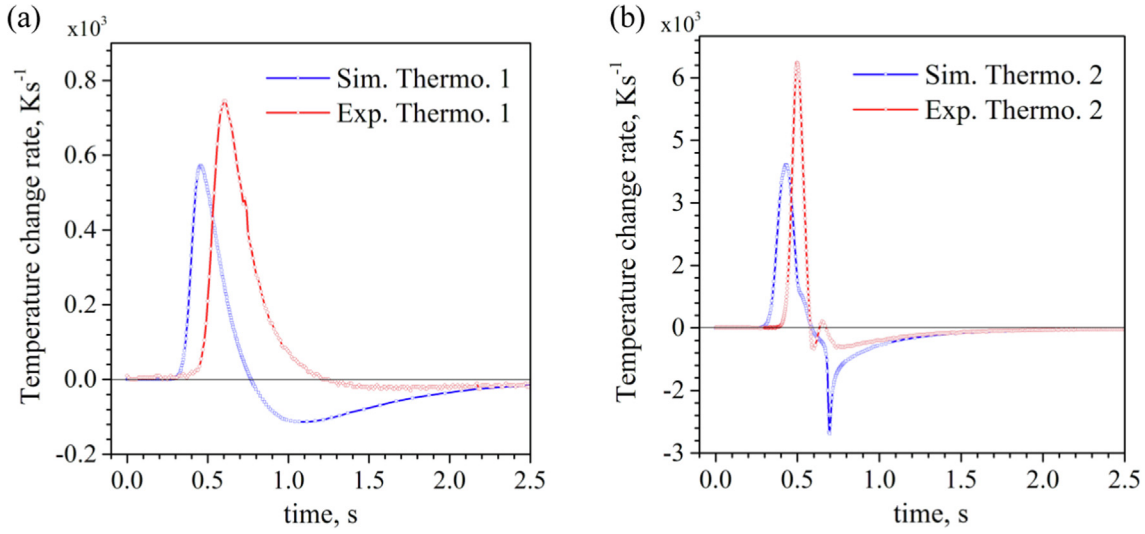

Fig. 13. Comparative of temperature change rate with the time of experimental and modelled specimens in the position of (a) Thermocouple 1 and (b) Thermocouple 2, (according to Fig. 12b) for Line 1 laser conditions.

ment to within 10% for most cases (Table 2). This prediction of spatial extent using the model is equivalent to a peak temperature isotherm equal to A_f, and given its importance in the engineering of these mesostructured zones, this is considered a strong validation for the applicability of the model. The remaining deviation between the experiment and model at the 800 K isotherm can be explained by: 1) the experimental error in the measurement of the zones estimated in the order of ±0.1 mm, 2) the simulated results correspond to a static reference A_f temperature at 100 K/s, which can vary around 45 K in the heating rate range from 1 K/s to 30•103 K/s [25], affecting the extent of the regions as predicted by the thermal model, 3) imprecisions inherent in the model settings, in particular in the uncertainty of absorptivity, which has demonstrated to have a strong effect on the simulated temperature field as depicted in Fig. 11b.

Another source of error may lay in the exclusion of some coupling effects by the model. The temperature field along the cross-section of Line 1 predicted by the model is superimposed on a light optical micrograph in Fig. 9a. A_s and A_f isotherms are delineated in white. The predicted intercritical region is in good agreement with the darkly etched microstructure. However, the dark etched region seems to intrude in the predicted full austenitisation region and austenite is marked by features resembling martensite as shown in Fig. 9b. Despite the model accounting for coupling effects between temperature and microstructure, it does not consider coupling effects between the stress fields and microstructure. Dagbert *et al.* [31], showed that austenite exhibits instability upon application of strain in several Fe–Ni–C alloys ranging in the composition of the present alloy. Matsumoto *et al.* [32], related local stress field in austenite and variant selection in deformation-induced martensitic transformation in Fe–24Ni–0.3C alloy. It is reasonable to assume that stress develops during the laser treatment close to the interface between austenitic and martensitic regions due to a mismatch in thermal expansion coefficients. This stress will provide an extra driving force for the formation of martensite, which might also explain discordances between the microstructure at the LAZ and the predicted temperature field.

A comparison between model-estimated and experimentally-determined heating rates can be made based on the thermocouple measurements presented in Fig. 13. It is apparent that at both locations where measurements were made, the model predicts lower peak heating rates, with experimental results 30–40% higher than

predicted. Although these measurements were only carried out on a 1 mm workpiece, where the effect of total heat input on heating rate will be significantly higher due to the reduced bulk available for heat dissipation, this does suggest for the model in general that thermal properties, primarily heat conductivity, should be improved to establish a better estimate of heating rate.

In conclusion and based on available evidence in light of experimental results, the model predictions of the temperature field can be considered accurate enough for further analysis on the optimization of process parameters and a better understanding of the microstructures developed at LAZ.

5.2. Effect of process parameters

Results obtained from the range of microstructures formed in the factorial design and thermal model highlight the importance of choosing the correct combination of laser processing parameters. Additionally, material and surface characteristics, like specimen absorptivity, and workpiece geometry should be considered to control the width and depth of the austenitic regions in austenite/martensite patterned mesostructured materials.

One notable effect of the variation in laser process parameters should be the extent of the LAZ. The linear energy (Table 1) of Line 1 and Line 2 are similar, but despite a marked increase in E_L for Line 3 and Line 4, only Line 4 shows a marked increase in the width and depth of the LAZ. In contrast to the monotonous increase in E_L, Fig. 11a shows a substantial difference in thermal field geometry when comparing Line 1 and Line 2 to Line 3 and Line 4. The radial symmetry and lack of a 'comet's tail' in the thermal field of Line 3 and Line 4 shows that, relative to the workpiece velocity, the heat has ample time to dissipate evenly in the low P, low v laser lines. This change will influence the assumed process efficiency (Eq. (2)), given that the dissipation of heat over comparatively large distances will reduce the heat available for the microstructural processes that determine the extent of the LAZ. A similar effect is observed in laser weld pools [33], where the critical timescale is related to convective flow in the weld pool. A decreased process efficiency can reasonably be assumed to result in a similar E_L for Line 3, compared to Line 1 and Line 2. The larger extent of Line 4 is a direct result of its significantly higher nominal (η = 1) E_L.

The achievable minimum width of the austenite region in the patterned microstructures proposed in this work will not only depend on the technical capacity to reduce the laser spot size but on the laser power and workpiece speed. The width of the austenite region becomes closer to the laser spot size as the laser power is reduced and the speed is increased, i.e. the heat input per area per unit time is reduced. This combination of laser parameters also results in steep thermal gradients, which are in principle desired to minimise the transition region between the austenite and base martensite microstructure. However, the penetration depth of the LAZ is strongly reduced as the laser power is reduced and the workpiece speed is increased.

Another important parameter influencing the LAZ is the specimen thickness. The changes in the LAZ for identical laser process parameters applied to different thickness is related to the heat diffusivity into the bulk of the material. Due to the high thermal conductivity of metals, the conductive heat flow within the bulk is orders of magnitude larger than heat transfer to surrounding media (e.g. air, working surfaces), especially at the short timescales under consideration in laser or inductive heating. Therefore, when a significant amount of bulk is available, the heat will spread quickly, to such an extent that 1) high cooling rates are achieved, and 2) only a limited amount of the sample is influenced enough by the heat to change its microstructure. Hung et al. [34], referred to this phenomenon as self-quenching and used it as the basis for the surface hardening of AISI 1045. Self-quenching relies on rapid and limited heat input, which locally alters microstructures, being dissipated into the bulk metal rapidly enough to limit the influence of the heat treatment beyond a certain depth. A larger extent of the LAZ is observed in the direction of the sample thickness when the material bulk is limited, as illustrated in Fig. 12a. This mechanism results in a pronounced influence of the sample geometry on the processing window of a localised laser heat treatment.

Finally, the absorptivity of the specimen has a strong influence on the temperature field and can be altered by changing the surface roughness or applying masks. The combination of laser parameters, specimen thickness and specimen absorptivity will determine the aspect ratio between width and depth. The minimisation of the microstructure transition region by an optimal combination of process parameters will be evaluated in future work.

5.3. Gradient microstructures at LAZ.

Meshkov and Pereloma [10], reviewed the martensite-to-austenite transformation mechanisms of Fe–Ni–C alloys. The resulting microstructure varies depending on the transformation mechanism, which is strongly influenced by the heating rate and composition. Shirazi et al. [35], reported a displacive mechanism in a Fe–23Ni alloy even at relatively low heating rates of 100 K/s. Apple and Krauss [25], analysed the change of A_s and A_f temperatures and microstructures depending on the heating rate in a steel composition similar to that in the present study. They suggested a pseudo-displacive martensite to austenite transformation mechanism at heating rates higher than 3000 K/s.

Fig. 14 shows simulated temperature change rate curves at different depths in the centre of the laser beam trajectory for the Line 1 condition. The temperature change rate varies markedly with depth indicating steep gradients along the specimen thickness. Maximum heating rates range the 5000–25,000 K/s within the LAZ depth. According to the experimental results, the actual heating rates can be even higher. At these high heating rates, martensite to austenite transformation in Fe–Ni–C alloy might occur by displacive or pseudo-displacive mechanisms in the whole laser-affected zone.

Austenite formation by displacive transformation mechanisms leads to austenite grains that reproduce the prior austenite grains concerning the shape, size and orientation, which is typically referred to as the memory effect. The memory effect was observed in FeNiC alloys [15,36] in which reverted austenite grains develop a

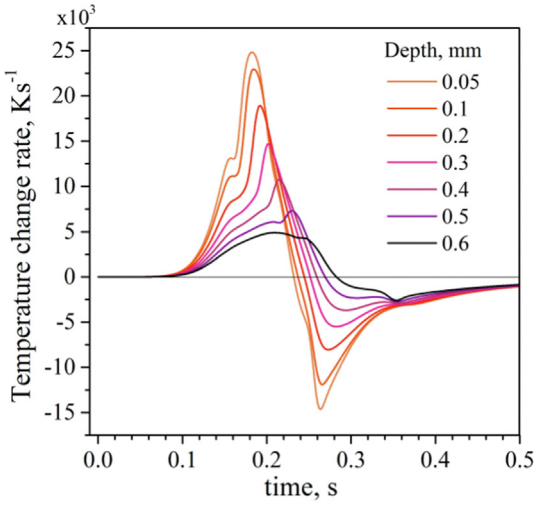

Fig. 14. Modelled temperature change rate with the time of 1 mm specimen at different depths for Line 1 laser conditions.

higher dislocation density than that for initial grains, which is likely inherited from the martensite. Depending on the achieved temperature and time, the freshly transformed austenite grains under displacive mechanisms might exhibit partial recovery of these dislocations or recrystallization, resulting in fine austenite grains replacing larger recovered ones [36].

Two well-differentiated austenitic microstructures were observed at the surface of LAZ in all laser lines (Fig. 7 and Fig. 8). Fine austenite grains were formed in the region most directly affected by the laser beam, Z1, usually larger than the laser spot size. Coarse grains were formed in the region close to the interface with the martensitic base microstructure. These coarse austenite grains matched well with the initial austenitic microstructure and with the assumption of a displacive mechanism of transformation when adhering to the proposed memory effect. Fine grains are presumed to be recrystallised grains and thus Z1 can be considered to display locations in which temperatures higher than the recrystallisation temperature were reached. The simulated temperatures at the distance delimiting Z1 for Lines 1 to 4 conditions are in the range of 1315 K to 1415 K (see Table 2). Heat-treated dilatometry specimens below 1173 K did not show a recrystallized structure. However, recrystallized austenite grains were sporadically observed in specimens heated above 1173 K (see Fig. 6b).

The smooth decrease in hardness with increasing peak temperature measured in dilatometry specimens below the 1173 K is likely explained by the initiation of dislocation recovery in austenitic microstructures. In line with the results of Apple and Krauss [25], a diffusive mechanism likely occurs upon 100 K/s heating in a dilatometry specimen. This should lead to a lower density of dislocations, and thus to a lower hardness, compared to a more displacive transformation character at LAZ. Similarities in hardness profile along the width and depth of the Z2 region to those measured in dilatometry specimens are explained by several factors. In the dilatometry specimen, carbon content is close to the nominal composition. Higher carbon content in the austenite will counteract the possible decrease in hardness by reduction of dislocations in the austenite at the bulk of the dilatometry specimen. Decarburisation is to some extent expected in the Z2 region at the LAZ surface, although a priori, this should not be the case in the Z2 region at LAZ depth. However, high heating rates at LAZ might also result in incomplete carbide dissolution, as discussed by Meshkov and Pereloma [10]. Incomplete carbide dissolution would not only explain the hardness values but supports the theory of a displacive mechanism. The observation of carbides might require special characterisation, which is not the scope of the present work.

The sudden drop in hardness above the 1173 K in dilatometry specimens matched well with the initiation of recrystallisation. This situates the recrystallisation temperature 200 K below that estimated in the laser-treated specimens. The high population of small grains in the Z1 region at LAZ compared to dilatometry specimens suggest that recrystallisation is completed in the former and just only initiated in the last. This would be in agreement with the high predicted temperatures at LAZ at which full recrystallisation would be achieved. The current state-of-the-art application of ultrafast heating to steel (in the range of 1000 K/s) shows a noteworthy influence on the heating rate in the recrystallisation of steel microstructures. Castro Cerda et al. [37] and Li et al. [38] evidenced that, although the recrystallisation onset temperature remains barely unaltered by the heating rate in low carbon steel, the recrystallisation fraction with temperature curve is slightly shifted to higher temperatures when the heating rate increases. Valdes-Tabernero et al. [39], showed that recrystallised fraction is affected by soaking time after ultrafast heating of low-carbon steel. In the present study, large differences in heating rates justify the divergences between the recrystallisation temperatures obtained by dilatometry experiments and that combining the thermal model with the observation of microstructures at LAZ. An equivalent hardness is obtained in Z1 at LAZ surface and dilatometry specimens despite the marked differences in grain size. Besides the obvious differences in recrystallization completion, which will affect the dislocation density of austenite, decarburization near the surface of LAZ would counteract the effect of small austenite grain size on increasing hardness.

The possible occurrence of pseudo-displacive martensite to austenite transformation mechanisms and austenite recrystallization have been shown to strongly influence the austenite hardness. This will be reflected in its work hardening and mechanical stability upon deformation. The observed progressive hardness transition from austenite to base martensite might be positive for a more effective stress and strain transfer between the austenite and martensite, enhancing the macroscopic properties of mesostructured austenite/martensite steels [40]. This gradual transition is not only achieved by the differences observed in the austenite microstructures affected by the steep peak temperature and heating rate gradients, as previously discussed. Below A_s, the decrease of hardness in martensitic microstructures with temperature is a reflection of increasing martensite tempering. The decrease of hardness measured upon heating from temperatures in the range of 473 K to 773 K in dilatometry specimens (Fig. 5) matches well with the hardness fluctuation measured from the base material to the dark etched regions of different laser lines, Z3 in Fig. 7, Fig. 8 and Fig. 9c. The severity of tempering will be influenced by the time the specimen is exposed to temperatures in the tempering range and will vary depending on the heating and cooling rates achieved. The agreement between the hardness of dilatometry and laser-treated specimen evidence that short tempering times can have a significant local influence on the martensite microstructure and properties.

This work provides a comprehensive vision of how the extent of austenite and tempered martensite regions can be engineered in a base martensitic microstructure by varying the localised laser treatment process parameters. It is common knowledge in brazing that the geometry of the joint of two materials with dissimilar strength influences the yield and uniform tensile stresses of the weak material, leading to values several times higher than that of the material alone [41]. These effects can be exploited in large mesostructure steel components with enhanced properties, in which the application of laser treatments can be straightforwardly industrialized at the finished part level for such purposes. The topology of the mesostructure can be varied to enhance the deformation mechanisms of the different phases, resulting in improved mechanical performance in terms of, e.g., energy absorption and tolerance to damage. Hence, mesostructured steel will find many applications in sectors such as the automotive industry, aerospace and energy production or transportation.

6. Conclusions

Austenite/martensite mesostructures can be created in Fe–Ni–C steel by solid-state transformations using localised laser heat treatments. A processing window was established based on the analysis of resulting microstructures after the variation of laser parameters, which was supported by heat treatments at a dilatometer and the formulation of a thermal model. The following conclusions were extracted:

- A gradient microstructure showing a complex interplay between martensite tempering, martensite to austenite phase transformation dynamics, recovery and recrystallisation is developed along the laser-affected zone.

- The extent of different microstructure zones can be tailored by varying laser parameters, specimen thickness and absorptivity.
- The instantaneous metallo-thermal coupling implemented in the proposed thermal model, in conjunction with the phase change hysteresis for thermal parameters, predicted temperature fields that were in good agreement with the resulting microstructures at the LAZ and experimental temperature measurements. The model exhibited a high sensitivity to variations in absorptivity, which is in agreement with the experiments and requires careful calibration for any future work. Coupling effects related to residual stresses developed in the austenite/martensite interface regions should be also considered in the design of novel patterned mesostructured metal alloys.
- Heating rates as high as 25000 K/s were predicted close to the laser spot, which in addition to observed austenitic microstructure at LAZ indicate that martensite to austenite transformation occurs by a pseudo-displacive mechanism and that austenite is then fully recrystallised if the recrystallisation temperature is exceeded.

Data availability

The raw/processed data required to reproduce these findings cannot be shared at this time due to technical or time limitations, though will be published alongside Data in Brief article and shared on request.

Declaration of Competing Interest

The authors declare that they have no known competing financial interests or personal relationships that could have appeared to influence the work reported in this paper.

Acknowledgements

The authors want to acknowledge Kees Kwakernaak, Jurriaan van Slingerland and Sander van Asperen from the Delft University of Technology, for their help and wise advice for the present work. The research leading to these results has received funding from the European Research Council under the European Union's Seventh Framework Programme (FP/2007–2013)/ERC Grant Agreement n. [306292].

References

[1] A.P. Mackwood, R.C. Crafer, Thermal modelling of laser welding and related processes: a literature review, Optics Laser Technol. 37 (2) (2005) 99–115, https://doi.org/10.1016/j.optlastec.2004.02.017.
[2] J. Mazumder, Laser heat treatment: the state of the art, JOM 35 (5) (1983) 18–26, https://doi.org/10.1007/BF03338273.
[3] B. Syed, S.M. Shariff, G. Padmanabham, S. Lenka, B. Bhattacharya, S. Kundu, Influence of laser surface hardened layer on mechanical properties of re-engineered low carbon steel sheet, Mater. Sci. Eng. A 685 (2017) 168–177, https://doi.org/10.1016/j.msea.2016.12.124.
[4] L. Orazi, A. Fortunato, G. Cuccolini, G. Tani, An efficient model for laser surface hardening of hypo-eutectoid steels, Appl. Surf. Sci. 256 (6) (2010) 1913–1919, https://doi.org/10.1016/j.apsusc.2009.10.037.
[5] J. Leunda, V. García Navas, C. Soriano, C. Sanz, Effect of laser tempering of high alloy powder metallurgical tool steels after laser cladding, Surf. Coat. Technol. 259 (2014) 570–576, https://doi.org/10.1016/j.surfcoat.2014.10.028.
[6] S.V. Telrandhe, J. Bhagyaraj, S. Mishra, S. Karagadde, A new approach to control and optimize the laser surface heat treatment of materials, J. Mater. Process. Technol. 262 (2018) 492–502, https://doi.org/10.1016/j.jmatprotec.2018.07.017.
[7] A.O. Andreev, D.P. Bykovskiy, A.V. Osintsev, V.N. Petrovskiy, I.I. Ryashko, E.N. Blinova, et al., Effect of the laser heat treatment on the formation of the gradient structures in alloys based on Fe–Cr–Ni system, J. Phys.: Conf. Ser. 941 (2017) 12027, https://doi.org/10.1088/1742-6596/941/1/012027.
[8] E.V. Pimenov, Possibilities of using a local heat treatment to produce new precision alloys, Steel Transl. 49 (9) (2019) 649–651, https://doi.org/10.3103/S0967091219090109.
[9] H.J. Breukelman, M.J. Santofimia, J. Hidalgo, Hierarchically patterned multiphase steels created by localised laser treatments, Mater. Des. 221 (2022), https://doi.org/10.1016/j.matdes.2022.110984 110984.
[10] Y.Y. Meshkov, E.V. Pereloma, The effect of heating rate on reverse transformations in steels and Fe–Ni-based alloys, in: Phase Transformations in Steels, Elsevier, 2012, pp. 581–618.
[11] G. Krauss, Fine structure of austenite produced by the reverse martensitic transformation, Acta Metall. 11 (6) (1963) 499–509, https://doi.org/10.1016/0001-6160(63)90085-3.
[12] A. Takimoto, S. Yoshinaka, Y. Nakamichi, Analysis of strengthening due to deformation-induced martensitic transformation in a Fe–Ni–C steel, Trans. JSME 56 (521) (Ser.A 1990,) 113–120, https://doi.org/10.1299/kikaia.56.113.
[13] V.A. Teplov, G.A. Pegushina, R.I. Kuznetsov, Plasticity of metastable austenitic Fe–Ni–C steels and deformation-induced martensite structure under hydrostatic tension, Fiz. Met. Metalloved (USSR) 60(2) 1985.
[14] Y. Tomota, K. Tanabe, K. Kuroki, I. Tamura, On the ductility of martensite in an ausformed Fe–Ni–C Alloy, 日本金属学会誌 41 (3) (1977) 313–319, https://doi.org/10.2320/jinstmet1952.41.3_313.
[15] A. Alaei, H. Jafarian, A.R. Eivani, Observation austenite memory and significant enhancement of tensile properties during cyclic reverse martensite transformation in a Fe–Ni–C TRIP steel, Mater. Sci. Eng. A 676 (2016) 342–350, https://doi.org/10.1016/j.msea.2016.09.003.
[16] T. Miura, R. Ueji, H. Fujii, Enhanced tensile properties of Fe–Ni–C steel resulting from stabilization of austenite by friction stir welding, J. Mater. Process. Technol. 216 (2015) 216–222, https://doi.org/10.1016/j.jmatprotec.2014.09.014.
[17] N.S. Bailey, W. Tan, Y.C. Shin, Predictive modeling and experimental results for residual stresses in laser hardening of AISI 4140 steel by a high power diode laser, Surf. Coat. Technol. 203 (14) (2009) 2003–2012, https://doi.org/10.1016/j.surfcoat.2009.01.039.
[18] R. Patwa, Y.C. Shin, Predictive modeling of laser hardening of AISI5150H steels, Int J Mach Tool Manu 47 (2) (2007) 307–320, https://doi.org/10.1016/j.ijmachtools.2006.03.016.
[19] T. Mioković, V. Schulze, O. Vöhringer, D. Löhe, Prediction of phase transformations during laser surface hardening of AISI 4140 including the effects of inhomogeneous austenite formation, Mater. Sci. Eng. A 435–436 (2006) 547–555, https://doi.org/10.1016/j.msea.2006.07.037.
[20] J. Goldak, A. Chakravarti, M. Bibby, A new finite element model for welding heat sources, MTB 15 (2) (1984) 299–305, https://doi.org/10.1007/BF02667333.
[21] H. Breukelman, M.J. Santofimia, J. Hidalgo, Dataset of a thermal model for the prediction of temperature fields during the creation of austenite/martensite mesostructured materials by localized laser treatments in a Fe–Ni–C alloy. Data in Brief, 2022, Under review.
[22] C.A. Schneider, W.S. Rasband, K.W. Eliceiri, NIH Image to ImageJ: 25 years of image analysis, Nat. Methods 9 (7) (2012) 671–675, https://doi.org/10.1038/nmeth.2089.
[23] M. Umemoto, I. Tamura, The morphology and substructure of butterfly martensite in ferrous alloys, J. Phys. Colloques 43(C4) (1982) C4-523–C4-528, 10.1051/jphyscol:1982481.
[24] H. Sato, S. Zaefferer, A study on the formation mechanisms of butterfly-type martensite in Fe–30% Ni alloy using EBSD-based orientation microscopy, Acta Mater. 57 (6) (2009) 1931–1937, https://doi.org/10.1016/j.actamat.2008.12.035.
[25] C. Apple, G. Krauss, The effect of heating rate on the martensite to austenite transformation in Fe–Ni–C alloys, Acta Metall. 20 (7) (1972) 849–856, https://doi.org/10.1016/0001-6160(72)90077-6.
[26] H. Bhadeshia, R. Honeycombe, Steels: Microstructure and Properties, Fourth Edition., Elsevier Science and Technology Books, Inc, 2017 [Place of publication not identified]:.
[27] G. Casalino, M. Mortello, S.L. Campanelli, Ytterbium fiber laser welding of Ti6Al4V alloy, J. Manuf. Process. 20 (2015) 250–256, https://doi.org/10.1016/j.jmapro.2015.07.003.
[28] I. Tomashchuk, P. Sallamand, E. Cicala, P. Peyre, D. Grevey, Direct keyhole laser welding of aluminum alloy AA5754 to titanium alloy Ti6Al4V, J. Mater. Process. Technol. 217 (2015) 96–104, https://doi.org/10.1016/j.jmatprotec.2014.10.025.
[29] F. Forouzan, A. Kermanpur, A. Najafizadeh, A. Hedayati, Processing of nano/submicron grained stainless steel 304L by an advanced thermomechanical process, Int. J. Mod. Phys. Conf. Ser. 05 (2012) 383–390, https://doi.org/10.1142/S2010194512002267.
[30] D. Bergström, J. Powell, A.F. Kaplan, The absorption of light by rough metal surfaces—a three-dimensional ray-tracing analysis, J. Appl. Phys. 103 (10) (2008), https://doi.org/10.1063/1.2930808 103515.
[31] C. Dagbert, M. Sehili, P. Gregoire, J. Galland, L. Hyspecka, Mechanical study of instability of austenitic FeNiC alloys—effect of hydrogen, Acta Mater. 44 (7) (1996) 2643–2650, https://doi.org/10.1016/1359-6454(95)00401-7.
[32] A. Matsumoto, M. Chen, A. Shibata, T. Miyazawa, M. Sato, N. Tsuji, Relationship between local stress field in austenite and variant selection in deformation-induced martensitic transformation in Fe-24Ni-0.3C alloy, Mater. Today:. Proc. 2 (2015) S945–S948, https://doi.org/10.1016/j.matpr.2015.07.438.
[33] C. Lampa, J. Powel, A. Ivarson, C. Magnusson, Factors affecting the efficiency of laser welding, Lasers Eng. 4 (1995) 73–83.
[34] T.-P. Hung, H.-E. Shi, J.-H. Kuang, Temperature modeling of AISI 1045 steel during surface hardening processes, Materials (Basel) 11 (10) (2018), https://doi.org/10.3390/ma11101815.

[35] H. Shirazi, G. Miyamoto, S. Hossein Nedjad, T. Chiba, M. Nili Ahmadabadi, T. Furuhara, Microstructure evolution during austenite reversion in Fe–Ni martensitic alloys, Acta Mater. 144 (2018) 269–280, https://doi.org/10.1016/j.actamat.2017.10.068.
[36] V.I. Zel'dovich, Three mechanisms of formation of austenite and inheritance of structure in iron alloys, Met. Sci. Heat Treat. 50 (9–10) (2008) 442–448, https://doi.org/10.1007/s11041-009-9082-3.
[37] F.M. Castro Cerda, F. Vercruysse, T.N. Minh, L. Kestens, A. Monsalve, R. Petrov, The effect of heating rate on the recrystallization behavior in cold rolled ultra low carbon steel, Steel Res. Int. 88(1):1600351 (2017), https://doi.org/10.1002/srin.201600351.
[38] P. Li, J. Li, Q. Meng, W. Hu, D. Xu, Effect of heating rate on ferrite recrystallization and austenite formation of cold-roll dual phase steel, J. Alloy. Compd. 578 (2013) 320–327, https://doi.org/10.1016/j.jallcom.2013.05.226.
[39] M.A. Valdes-Tabernero, C. Celada-Casero, I. Sabirov, A. Kumar, R.H. Petrov, The effect of heating rate and soaking time on microstructure of an advanced high strength steel, Mater. Charact. 155 (2019), https://doi.org/10.1016/j.matchar.2019.109822 109822.
[40] T. Koseki, J. Inoue, S. Nambu, Development of multilayer steels for improved combinations of high strength and high ductility, Mater. Trans. 55 (2) (2014) 227–237, https://doi.org/10.2320/matertrans.M2013382.
[41] W.G. Moffatt, J. Wulff, Strength of silver brazed joints in mild steel, JOM 9 (4) (1957) 442–445, https://doi.org/10.1007/BF03397896.